

# Amorphous Boron Nitride as an Ultrathin Copper Diffusion Barrier for Advanced Interconnects

Onurcan Kaya<sup>1,2,3</sup>, Hyeongjoon Kim<sup>4,5</sup>, Byeongkyu Kim<sup>6</sup>,  
Thomas Galvani<sup>1</sup>, Luigi Colombo<sup>7</sup>, Mario Lanza<sup>8</sup>, Hyeon-Jin  
Shin<sup>9</sup>, Ivan Cole<sup>2</sup>, Hyeon Suk Shin<sup>5,10,11</sup>, and Stephan Roche<sup>1,12</sup>

<sup>1</sup> Catalan Institute of Nanoscience and Nanotechnology (ICN2), CSIC and BIST, Campus UAB, Bellaterra, 08193, Barcelona, Spain

<sup>2</sup> School of Engineering, RMIT University, Melbourne, Victoria, 3001, Australia

<sup>3</sup> Department of Electronic Engineering, Universitat Autònoma de Barcelona (UAB), Campus UAB, Bellaterra, 08193 Barcelona, Spain

<sup>4</sup> Department of Chemistry, Ulsan National Institute of Science and Technology, Ulsan 44919, Republic of Korea

<sup>5</sup> Center for 2D Quantum Heterostructures, Institute for Basic Science (IBS), Suwon16419, Republic of Korea

<sup>6</sup> School of Semiconductor Materials and Devices Engineering, Ulsan National Institute of Science and Technology (UNIST), Ulsan 44919, Republic of Korea

<sup>7</sup> CNMC, LLC, Dallas, TX, 75248, USA

<sup>8</sup> Department of Materials Science and Engineering, National University of Singapore, 117575, Singapore

<sup>9</sup> Department of Semiconductor Engineering, School of Electrical Engineering and Computer Science, Gwangju Institute of Science and Technology (GIST), Republic of Korea

<sup>10</sup> Department of Energy Science, Sungkyunkwan University (SKKU), Suwon 16419, Republic of Korea

<sup>11</sup> Department of Chemistry, Sungkyunkwan University (SKKU), Suwon 16419, Republic of Korea

<sup>12</sup> ICREA Institutio Catalana de Recerca i Estudis Avancats, 08010 Barcelona, Spain

E-mail: [stephan.roche@icn2.cat](mailto:stephan.roche@icn2.cat)

**Abstract.** This study focuses on amorphous boron nitride ( $\alpha$ -BN) as a novel diffusion barrier for advanced semiconductor technology, particularly addressing the critical challenge of copper diffusion in back-end-of-line (BEOL) interconnects. Owing to its ultralow dielectric constant and robust barrier properties,  $\alpha$ -BN is examined as an alternative to conventional low-k dielectrics. The investigation primarily employs theoretical modelling, using a Gaussian Approximation Potential, to simulate and understand the atomic-level interactions. This machine learning-based approach allows the performance of realistic simulations of amorphous structure of  $\alpha$ -BN, enabling the exploration of the impact of different film morphologies on barrier efficacy. Furthermore, we studied the electronic and optical properties of the films using a simple Tight-Binding model. In addition to the theoretical studies, we performed diffusion studies of copper through PECVD  $\alpha$ -BN on Si. The results from both the theoretical and experimental investigations highlight the potential of  $\alpha$ -BN as a highly effective diffusion barrier, suitable for integration in nanoelectronics. This research shows that

$\alpha$ -BN is a promising candidate for BEOL interconnects but also demonstrates the synergy of advanced computational models and experimental methods in material innovation for semiconductor applications.

## 1. Introduction

The continuous down-scaling of devices and architectures has been the major goal of the electronic industry for decades in order to increase performance, chip density, and reduce power consumption [1, 2, 3]. Interconnect technology is also experiencing significant challenges as devices are scaled down, with sustained efforts to decrease the resistance of metals and to lower the dielectric constant of intermetal dielectrics (IMDs), for optimised control of signal delays such as RC delay. The diffusion barrier that prevents the interaction between metals and IMD is also becoming thinner and is required to have excellent blocking properties. Ultimately, the technology aims for an almost “barrier-free” structure. Two-dimensional (2D) materials, such as MoS<sub>2</sub> and h-BN have recently garnered attention as potential barrier materials. Indeed, recent studies have shown that MoS<sub>2</sub>, when synthesized through Atomic Layer Deposition (ALD), can act as an effective Cu diffusion barrier, potentially reducing barrier thickness down to 1-2 nm [4, 5, 6]. Furthermore, the integration of dopants into MoS<sub>2</sub> such as Niobium (Nb) has been found to enhance its ability to block Cu atom diffusion, indicating its suitability for sub-5 nm technology nodes. However, while these 2D materials could act as efficient diffusion barriers, they also have a higher dielectric constant which would add to the RC delay.

Hexagonal boron nitride (h-BN), on the other hand, could be a better choice due to its low dielectric constant and higher bandgap. However, the practical application of these 2D materials is confronted with significant challenges. Integrating these materials into existing semiconductor manufacturing processes, especially developing a BEOL-compatible growth process for deposition on dielectrics remains a major challenge [7, 8, 9]. Moreover, the presence of defects in 2D materials, such as vacancy defects in hBN and MoS<sub>2</sub>, can lead to Cu accumulation, creating diffusion pathways that compromise the barrier’s effectiveness [10]. Amidst the ongoing quest for materials that can meet the stringent demands of advanced semiconductor technologies, amorphous boron nitride ( $\alpha$ -BN) emerges as a particularly compelling candidate. In contrast to h-BN,  $\alpha$ -BN does not suffer from dangling bonds and grain boundaries. In addition to its low temperature growth,  $\alpha$ -BN films can be uniformly synthesized on various substrates (such as metals and dielectrics) with a controllable thickness. This makes  $\alpha$ -BN a desirable dielectric material and diffusion barrier [11, 12]. Besides,  $\alpha$ -BN has been reported to have a low dielectric constant as a result of poor dipole alignment due to its amorphous nature [13]. While Hong et al. [2] reported an ultralow dielectric constant of 1.7 for 3 nm PECVD-grown  $\alpha$ -BN. Glavin et al. [12] pointed out that homonuclear bonds may open conductive pathways and increase the dielectric constant. They measured a

device dielectric constant of atomic layer deposition (ALD)-grown  $\alpha$ -BN of 5.9 with a band gap of 4.5 eV [12]. Similarly, the dielectric constant of ALD grown  $\alpha$ -BN at 65 - 250 °C is between 4.3 - 9.0 which increases with faster cooling. They observed that faster cooling leads to N deficiency and higher oxygen contamination, causing midgap states and higher dielectric constant [14]. Lin et al.[15] achieved a dielectric constant of 2.1 for sub-10 nm  $\alpha$ -BN films by optimising the growth process and using borazine as a precursor. Meanwhile, Abbas et al.[16] reported dielectric constants of 2.61 - 5.88 for sputtered  $\alpha$ -BN films with thicknesses ranging between 12 nm and 800 nm[16]. Due to their low dielectric constant, good mechanical properties, and thermal stability,  $\alpha$ -BN films have already been shown to act as efficient metal diffusion barriers. While Hong et al. [2] showed that a 3 nm  $\alpha$ -BN film can stop Co diffusion at 600 °C, Kim et al. [17] found that 7-nm- $\alpha$ -BN film can stop Cu diffusion up to 500 °C. Hence,  $\alpha$ -BN seems to be the ideal dielectric material due to its ultralow dielectric constant and great barrier properties. However, as shown in the literature [12, 15, 14, 18, 19], the properties and performance of  $\alpha$ -BN are determined by their morphology. Hence, ALD  $\alpha$ -BN with the correct composition could be an ideal dielectric material due to the potential low dielectric constant and excellent metal barrier properties.

An exhaustive experimental investigation of the morphology and properties of  $\alpha$ -BN would be quite time consuming and expensive. On the other hand, atomistic simulations would allow us to study materials at the atomic level and can provide faster insights into the relation between morphology and key parameters of materials with moderate computational cost. Notwithstanding, implementing an accurate modelling of highly disordered materials such as  $\alpha$ -BN is quite a challenging task. Due to the lack of long-range order, the simulation box of amorphous materials should be quite large. This becomes quickly prohibitive for *ab initio* calculations. On the other hand, simulations using classical Molecular Dynamics (MD) with empirical potentials can deal with such large samples. However, due to simplifications and assumptions used to develop these interatomic potentials, classical MD cannot capture the diverse atomic environments of the amorphous material. These challenges can be overcome using machine learning-based approaches. Classical MD simulations with machine learning-based interatomic potential trained over *ab initio* calculations can deal with very large simulation boxes with *ab initio* accuracy [20, 21].

Here, the relationship between the morphology of  $\alpha$ -BN structures and their barrier properties is assessed both theoretically and experimentally. First, we develop a Gaussian Approximation Potential (GAP) model to describe the interactions between  $\alpha$ -BN and Cu atoms. Later, we generate  $\alpha$ -BN films with different thicknesses, and by employing different parameters, we investigate their resulting morphologies and barrier properties. We also study the mechanical properties of generated  $\alpha$ -BN samples, as well as their electronic and dielectric properties. Finally, we present an experimental investigation of the barrier performance of PECVD-grown 3-, 5-, and 7-nm thick  $\alpha$ -BN films against Cu diffusion to the Si-based substrate and compare it with the simulations.

## 2. Methods

This study combines both computational models and experimental techniques to evaluate the diffusion barrier potential of ultrathin amorphous boron nitride ( $\alpha$ -BN) films against copper (Cu). In our computational investigation, we used molecular dynamics (MD) simulations and a tight binding (TB) model to generate  $\alpha$ -BN samples with different qualities, calculate the mechanical and optical properties, and evaluate their diffusion barrier properties. Experimental efforts focused on the barrier properties of PECVD-grown  $\alpha$ -BN films of different thicknesses by detecting the presence of copper silicide crystals. Both experimental and computational work provide a good understanding of the effectiveness of  $\alpha$ -BN as a Cu diffusion barrier in future electronic applications.

### *2.1. Molecular Dynamics Simulations*

MD simulations use Newton’s law of motion to follow the trajectories of atoms through time. The accuracy and reliability of MD simulations largely depends on the accuracy of interatomic potentials. While there are several empirical potentials for  $\alpha$ -BN and Cu separately, there is no potential that takes both BN and Cu into account. Moreover, empirical potentials provide insufficient accuracy for such complex systems [20, 21, 22]. Machine learning based interatomic potentials that utilize a large dataset of quantum-mechanically computed reference data for structures, energies and forces are quite useful for disordered systems since they enable us to study large numbers of atoms with an accuracy comparable to DFT and a reasonable computing cost. Therefore, we trained a Gaussian Approximation Potential for BNCu systems that is based on DFT-generated energy and force data of a large database. The dataset contains isolated atoms, molecular compounds, crystalline structures, heterostructures and random structures. Details of training and validation of the GAP model are presented in Appendix A.

To generate  $\alpha$ -BN films with different qualities, we employed a melt-quench protocol. This protocol is an efficient way to generate amorphous structures and glasses in MD and has been used extensively by community [18, 19, 22]. In this protocol, an equal number of B and N atoms were placed in a cube simulation box which is periodic in all directions. However, we placed a 25 Å-thick vacuum region at both the top and bottom of the film to prevent boundary interactions and mimic thin films. After a minimization and an equilibration run at 5000 K for 20 ps with a timestep of 0.25 fs (same timestep used in all simulation), all films were cooled down with a constant cooling rate of 5 - 100 K/ps under NVT ensemble (constant volume-constant temperature) to systematically study the effect of cooling rates on film morphology, capturing variations in the degree of disorder characteristic of amorphous materials. Later all films are relaxed under NVE (constant volume-constant energy) and equilibrated under NVT ensemble for 20 ps each. Here, the initial density of each cube (before the addition of the vacuum regions) was fixed at approximately 2.1 g/cm<sup>3</sup>, the experimentally reported value for  $\alpha$ -BN films [2]. The number of atoms in 3-nm, 5-nm and 7-nm thick films are respectively 3000,

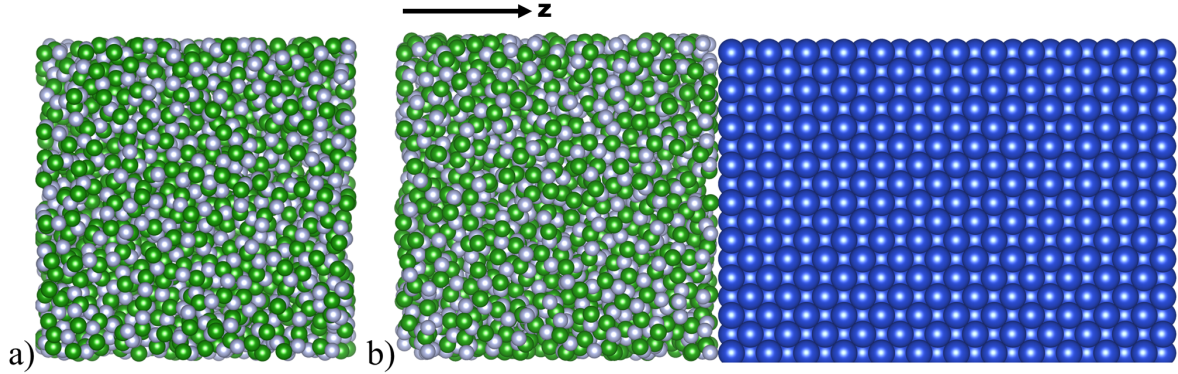


Figure 1: a) A sample of simulation box of 3-nm thick  $\alpha$ -BN films generated by a melt-quench protocol of the type used to calculate mechanical and dielectric properties; this structure was used for calculating mechanical and dielectric properties, b) a sample of simulation cells of 3-nm thick  $\alpha$ -BN/Cu heterostructures used for barrier calculations, where B, N, and Cu atoms are represented as green, white, and blue, respectively. Note that The z-axis, corresponding to the film thickness, is displayed horizontally in the figure for clarity. 2.5 nm thick vacuum spaces are applied to both of end of simulation cells, which are not shown here.

13000 and 37000 to maintain the selected density. Upon generating the films, several morphological features are investigated to evaluate the quality of samples. We checked the presence of  $sp^2$  and  $sp^3$  atoms, homonuclear bonds, nanovoids, as well as the density of the samples. We generated 5 samples at each thickness with each cooling rate to get statistically meaningful data. A 3-nm thick  $\alpha$ -BN sample generated using this protocol is shown in Fig.1-a.

Later, we investigated the mechanical properties of  $\alpha$ -BN thin films. The elastic constants of  $\alpha$ -BN thin films were calculated by computing the stress fluctuations and the Born matrix of  $\alpha$ -BN samples [23, 24, 25]. These simulations were performed over 100 ps, with data collected every 25 fs (100 steps), to obtain the complete elastic constant matrix for each sample. Mechanical properties (Young's modulus, bulk modulus, and shear modulus) were then derived from the elastic constants obtained in the MD simulations [26, 25].

5-nm thick Cu layers ( $z = 5$  nm) were placed atop the  $\alpha$ -BN films, as shown in Fig.1-b. Heterostructures were equilibrated and relaxed for 20 ps for each structure. Later the structures were heated up by 50 K with a constant rate of 5 K/ps, and then equilibrated at the target temperature for 50 ps and the positions of atoms were printed at every 10 fs. This cycle was performed under NVT ensemble. At the end of the equilibration run, the heterostructures were heated again. This cycle was continued until the temperature reached 1000 K. We evaluated the barrier performance of the films using mean squared displacement (MSD). MSD measures how much an atom moves from its initial position:  $MSD(t) = \langle r^{(i)}(t) - r^{(i)}(t = 0) \rangle$ . The slope of MSD is the diffusivity ( $D$ ) of atoms,  $D(t) = \lim_{t \rightarrow \infty} MSD(t)/6t$ . When the system is stable, diffusivity should ideally be zero

(or close to zero due to the temperature) [27]. When we observe an abrupt change in the diffusivity of Cu atoms, this means  $\alpha$ -BN cannot stop Cu atoms diffuse into the  $\alpha$ -BN barrier and potentially to the substrate material.

## 2.2. Tight Binding Model

To estimate the electronic properties and dielectric constant of  $\alpha$ -BN, we use a simple tight binding (TB) model based on a first nearest neighbors Slater-Koster approach [28]. The parameters of the model are fitted using data from the cubic, wurtzite, and single-layer hexagonal phases of BN at equilibrium and under 10% isotropic dilation, with B–B and N–N hoppings approximated using B–N parameters. While this model captures the effects of local coordination and geometry via distance-dependent hoppings, it lacks additional energetic corrections which could be important here [28].

We refer the reader to [28] and references therein for details and limitations, but for self-containedness, we outline the methodology here. Dielectric functions have been computed at  $T = 0$  K, at the single particle, frozen atoms level, in the long wavelength limit ( $\mathbf{q} \rightarrow 0$ ):[29]‡

$$\epsilon_1(\omega) = \text{Re}[\epsilon(\omega)] = 1 + \frac{16\pi}{\Omega} \frac{\hbar^2}{m_e^2} \sum_{v,c} \frac{|\langle c|\vec{\epsilon} \cdot \hat{\mathbf{p}}|v\rangle|^2}{(E_c - E_v)^2} \frac{E_c - E_v}{(E_c - E_v)^2 - (\hbar\omega)^2} \quad (1)$$

$$\epsilon_2(\omega) = \text{Im}[\epsilon(\omega)] = \frac{8\pi}{\Omega} \frac{\hbar^2}{m_e^2} \sum_{v,c} \frac{|\langle c|\vec{\epsilon} \cdot \hat{\mathbf{p}}|v\rangle|^2}{(E_c - E_v)^2} \delta(E_c - E_v - \hbar\omega) \quad (2)$$

in which  $\Omega$  is the system's unit cell volume,  $\hbar$  is the reduced Planck constant,  $m_e$  is the electron mass,  $\vec{\epsilon}$  is the polarization of the electric field,  $\omega$  its angular frequency, the  $E_i$  and  $|i\rangle$  are respectively the electronic eigenenergies and eigenstates of the TB Hamiltonian, with  $v$  and  $c$  running over the valence (occupied) and conduction (unoccupied) states, and  $\mathbf{p}$  is the momentum operator.

Eigenstates and eigenenergies were obtained by exact diagonalization of the TB Hamiltonian at the  $\Gamma$  point. Following the MD, periodic boundary conditions were assumed in  $(x, y)$  but not in  $z$ . Strictly, the unit cell height, and thus its volume,  $\Omega$ , is ill defined, as the films are two dimensional (and the unit cells thus contain arbitrary vacuum regions, as explained above) [30]. However, a natural choice of height is given here by the thickness of the films, through which a representative  $\Omega$  is thus prescribed.§ Matrix elements of the momentum operator were obtained as in [28], using a standard tight-binding approximation, which produces appropriate results for semiconductor systems [31, 32, 33, 34].

‡ In practice, we compute the complex dielectric function:  $\epsilon(\mathbf{q} = \mathbf{0}, \omega) = 1 + \frac{8\pi}{\Omega} \frac{\hbar^2}{m_e^2} \sum_{v,c} \frac{|\langle c|\vec{\epsilon} \cdot \hat{\mathbf{p}}|v\rangle|^2}{(E_c - E_v)^2} \left[ \frac{1}{E_c - E_v - \hbar\omega - i\eta} + \frac{1}{E_c - E_v + \hbar\omega + i\eta} \right]$  where  $\eta \rightarrow 0^+$  is a phenomenological broadening set here to  $k_b T_{room} = 26$  meV. The expressions given in the maintext are the  $\eta \rightarrow 0^+$  limits.

§ We use the difference  $\Delta z$  in  $z$  coordinate between the atom of highest and lowest  $z$  for unit cell height, and the  $(x, y)$  area  $\mathcal{A}$  of the periodic cell for the effective volume:  $\Omega \leftarrow \mathcal{A} \times \Delta z$ .

It has been suggested [28] that  $\alpha$ -BN can exhibit midgap states due to structural disorder and bond characteristics. These midgap states may increase the dielectric constant drastically since they allow low energy transitions. However, these states appear mostly localized in real space due to the effects of disorder in the samples. To visualize the formation of midgap states and these localization effects, we also calculated the electronic density of states (DOS)<sup>||</sup> and inverse participation ratio (IPR) for all eigenstates of each film. The IPR provides a measurement of a state's localization in real space. For an electronic eigenstate  $|\Psi\rangle$ , we adopt the definition  $\text{IPR}(|\Psi\rangle) = \sum_{\mathbf{n}} [q_{\mathbf{n}}(|\Psi\rangle)]^2$ , where the sum runs over atomic positions and  $q_{\mathbf{n}}(|\Psi\rangle)$  is the corresponding probability of presence of the electron at atomic site  $\mathbf{n}$  (obtained by summing the modulus squared of the projection of  $|\Psi\rangle$  on each of its orbitals). Heuristically, if  $|\Psi\rangle$  describes a state localized on a single atomic site, say  $\mathbf{m}$ ,  $q_{\mathbf{n}} \approx \delta_{\mathbf{n},\mathbf{m}}$  and  $\text{IPR}(|\Psi\rangle) \approx 1$ . On the other hand, if  $|\Psi\rangle$  describes a state delocalized over the whole system, the  $q_{\mathbf{n}}$  will be of order  $1/N_{\text{atoms}}$  and therefore  $\text{IPR}(|\Psi\rangle) \rightarrow 0$ .

### 2.3. Experimental Studies

**2.3.1.  $\alpha$ -BN Film Growth** To experimentally demonstrate the barrier properties of  $\alpha$ -BN samples, we employed capacitively coupled plasma-chemical vapor deposition (CCP-CVD) to deposit  $\alpha$ -BN films. The Si substrate was placed on a substrate holder in the deposition chamber. The substrate was heated at a rate of 10 °C/min and reached growth temperatures between 350 and 400 °C. Following a 20-minute annealing process, a borazine precursor ( $\text{B}_3\text{H}_6\text{N}_3$ , Gelest) was introduced into the chamber at a rate of 0.05 sccm with a hydrogen flow of 20 sccm. During the growth process, the plasma operated at a power of 20 W. The growth time was adjusted between 20 and 80 minutes depending on the thickness of the  $\alpha$ -BN film. After the growth was completed, the furnace was slowly cooled down to room temperature.

**2.3.2. Experimental Cu Diffusion Barrier Test** We assessed the Cu diffusion barrier properties of the grown  $\alpha$ -BN films. For comparison with simulation results, 3-nm, 5-nm, and 7-nm thick  $\alpha$ -BN films on Si substrate were prepared and a 50-nm thick Cu film was deposited on  $\alpha$ -BN/Si by e-beam evaporation. Cu/ $\alpha$ -BN/Si samples were annealed at the temperature range of 400 °C to 600 °C for 30 minutes using a vacuum furnace. Subsequently, these samples were immersed in a Cu etchant (49-1, Trensene) for 20 minutes to remove the Cu films, followed by a deionized water rinse. to remove the excess etchant. Cu diffusion was evaluated through confirmation of the formation of copper silicide using X-ray diffraction (XRD) and scanning electron microscopy (SEM).

<sup>||</sup> The DOS are computed using the same eigenenergies as the ones used for the dielectric function calculation, and with the same lorentzian broadening of 26 meV.

### 3. Properties of $\alpha$ -BN Thin Films

#### 3.1. Film Generation and Morphological Features

After generating samples through the melt-quench protocol, we first focused on key morphological features to identify the structural differences between fast- and slow-cooled structures. It is known that the morphology of  $\alpha$ -BN, as well as other disordered samples, determines the properties and performance of a device. [12, 18, 15, 28]. Therefore, a thorough investigation of morphological features is vital. In order to evaluate the “crystallinity vs. disorder” of the samples, we first computed the radial distribution function (RDF),  $\rho$ , of  $\alpha$ -BN films as a function of cooling rate. Fig. 2 presents the average RDF of 3-nm thick films (since all films show the same trend, only the 3-nm thick films are presented). While all structures are characterized by a clear and recognizable first two peaks, no peak can be identified for distances larger than 3 Å, indicating the absence of long-range order in the samples regardless of the cooling protocol employed and showing the amorphous character of the films is not affected by the cooling rate. The first peaks of the slow-cooled samples are close to 1.44-1.45 Å, which is the bond distance of  $sp^2$  B-N bonds, as can be seen in the close-up image of the first peak of the RDF presented in the inset of Fig. 2. The broad peak in the RDF indicates a

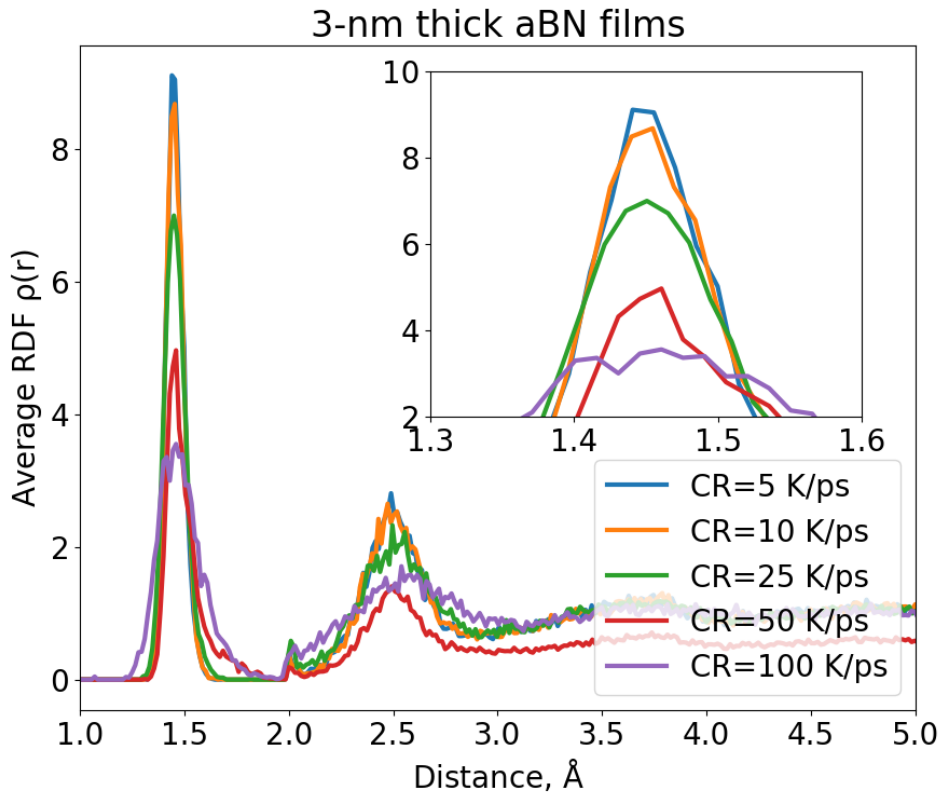


Figure 2: Radial distribution function of 3-nm thick  $\alpha$ -BN samples with respect to cooling rate (CR). Inset: the zoom-in to the first peak.



significant variation in bond lengths, reflecting a distribution between 1.35 and 1.55 Å, due to structural disorder. The peak becomes more broadened and shifted from 1.45 Å with higher cooling rates, indicating more disordered structures. Fig. 3 presents how several morphological features are changing due to the applied cooling rate. As shown in the figure, with higher cooling rates, the number of B-B bonds (which usually have a bond length of 1.6 - 1.8 Å) increased rapidly. Also, we observed that  $sp^1$ -hybridized atoms, since they are mostly located around voids and pinholes, have quite strongly varying bond distances, which also contributes to the broadening observed in the RDF.

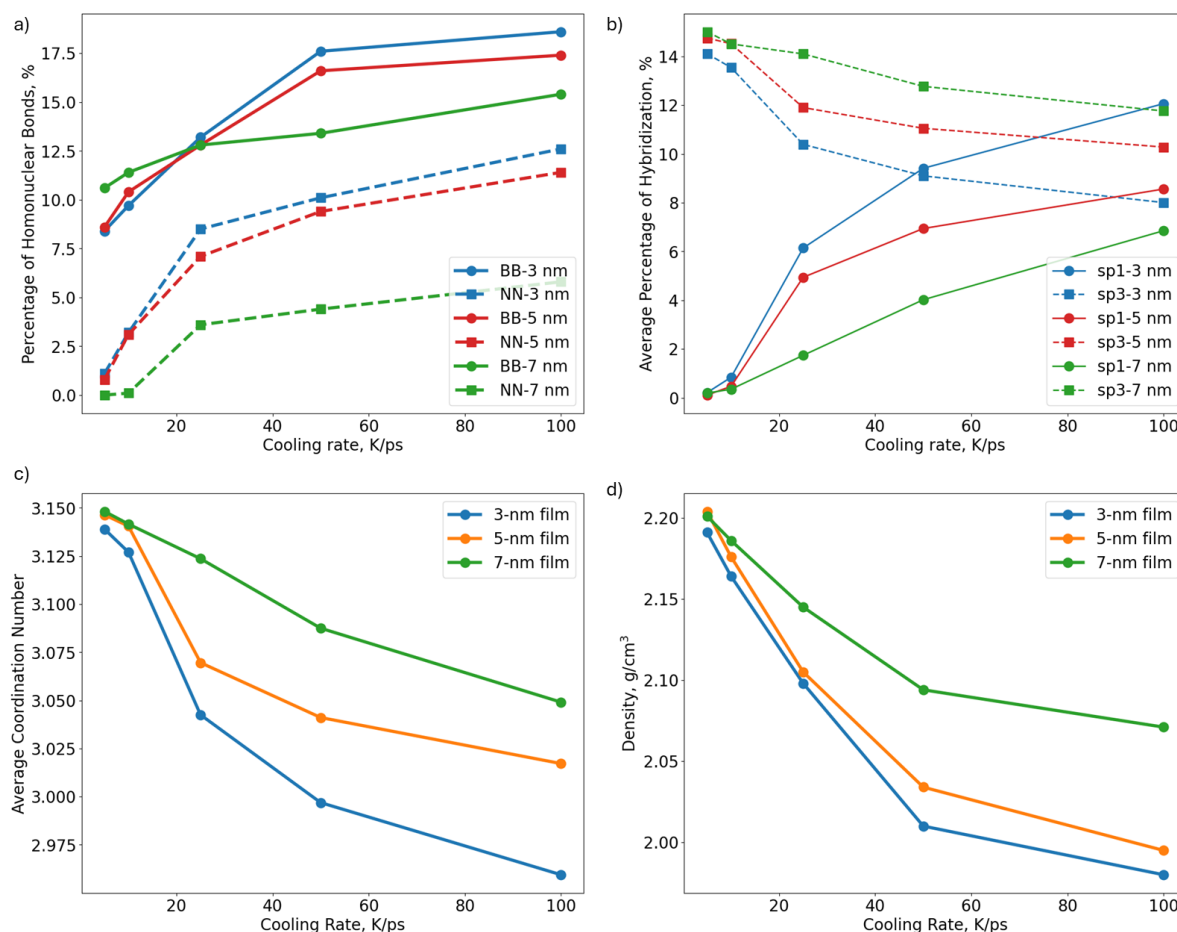


Figure 3: Variation of morphological features of  $\alpha$ -BN thin films with respect to the applied cooling rate: (a) percentage of homonuclear bonds (B-B + N-N bonds), (b) percentage of  $sp^1$ - and  $sp^3$ -hybridized atoms, (c) average coordination number, and (d) density. Each data point represents an average over five samples.

Fig. 3 presents many interesting trends between cooling rates and morphological features. Fig.3-a shows that higher cooling rates increase the proportion of both B-B and N-N bonds for all thickness. However, the amount of increase in homonuclear bonds varies across film thicknesses. For any given cooling rate, thinner samples consistently have more homonuclear bonds than thicker ones. For instance, the portions of

homonuclear bonds in 3-nm and 5-nm thick films generated at a cooling rate of 5 K/ps are approximately 10%, while this rises to 30% at higher cooling rates. In contrast, for rapidly cooled (cooling rate  $> 50$  K/ps) the 7-nm thick sample, the proportion of homonuclear bonds remains below 20 %. Fig. 3-b shows how the coordination number of  $\alpha$ -BN is influenced by applied cooling rates during film generation. Similarly to what we saw for homonuclear bonds, the effects of cooling rate on the local coordination numbers are more pronounced for thinner films. While all structures cooled at 5 K/ps have no  $sp^1$ -hybridized atoms (coordination number of 2), their proportion rapidly increases to 10% in 3-nm thick films at higher cooling rates. Similarly, for 5- and 7-nm thick films, the proportions of  $sp^1$ -hybridized atoms become  $\sim 8\%$  and  $\sim 6\%$ , respectively. Moreover, the number of  $sp^3$ -hybridized atoms (coordination number of 4) drops rapidly at all thicknesses as cooling rates increase. These changes in hybridization are also reflected in the average coordination number of the films, as shown in Fig. 3-c, where larger cooling rates result in a rapid decrease in average coordination for all thicknesses, most notably in the 3-nm thick films. While  $sp^1$ - and  $sp^3$ -hybridized fractions show opposing trends with the cooling rate, the average coordination number reflects the overall change in the local atomic environment. With larger cooling rates, the average coordination number of samples at all thicknesses drops quickly, with the largest change observed for 3 nm thick films. A parallel trend is also observed in density of the samples,<sup>¶</sup> as depicted in Fig. 3-d. The decrease in coordination number, as cooling rates increase, shows atoms getting far away from each other which leads lower density. While the density of films is  $\sim 2.21$  g/cm<sup>3</sup> for samples cooled with rate of 5 K/ps, the density drops even lower than 2 g/cm<sup>3</sup> for 3-nm and 5-nm thick films at higher cooling rate. Meanwhile, even the 7-nm thick samples generated with the largest cooling rate still has an average density of  $\sim 2.07$  g/cm<sup>3</sup>. The significant reduction in density, combined with the increasing number of  $sp^1$ -hybridized atoms suggests that fast-cooled films have more porous structures. Fig. B1 presented in Appendix B shows some voids observed in fast-cooled (with 50 K/ps and 100 K/ps) 3-nm thick  $\alpha$ -BN films. Around these defects, we also observe a number of  $sp^1$ -hybridized atoms, which underlines the relationship between the existence of voids and  $sp^1$ -hybridized atoms.

The observed reduction in homonuclear bonds and  $sp^1$ -hybridized atoms with increasing thickness, as shown in Fig. 3, suggests enhanced structural relaxation in thicker films. Interestingly, this improvement in structural order becomes more pronounced in the 7-nm films compared to the 3-nm and 5-nm films, where the differences are relatively smaller. This significant improvement in the 7-nm films reflects the ability to better accommodate strain and achieve a more ordered atomic arrangement as thickness increases. Similar behaviour has been reported in the literature for amorphous systems [35, 36, 37], where larger volumes facilitate relaxation processes and reduce disorder.

<sup>¶</sup> Like for the dielectric function, we used the difference in z-coordinate  $\Delta z$  between the atoms of highest and lowest z and the  $(x, y)$  area  $\mathcal{A}$  of the periodic cell to estimate the film volume  $\mathcal{A} \times \Delta z$ .

### 3.2. Mechanical Properties

Having good mechanical properties is crucial for diffusion barriers, as low mechanical strength and Young's modulus complicate the integration process. Moreover, good mechanical properties indicate that the film can resist deformation under stress which is crucial for structural integrity during the operation [2, 38, 39]. As other properties, mechanical properties are strongly influenced by the morphological features and fabrication process of  $\alpha$ -BN films. Here, we investigated the Young's, bulk and shear moduli of  $\alpha$ -BN films by computing the elastic constants as a function of film thickness and cooling rate.

The elastic constants of each film were calculated as explained in the Methods section.

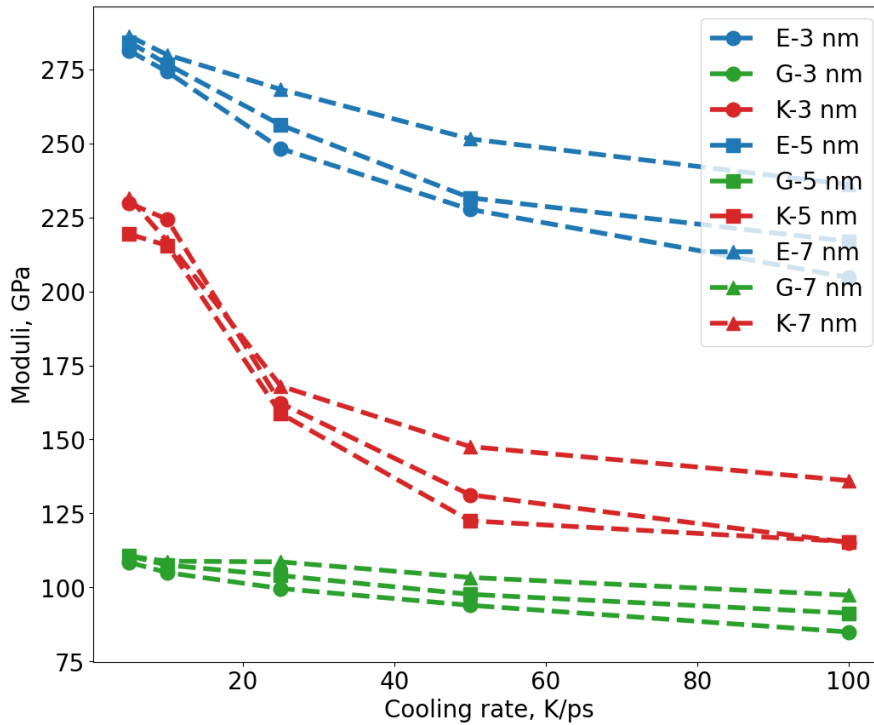


Figure 4: Young's modulus (E), shear modulus (G) and bulk modulus (K) of  $\alpha$ -BN films at different thicknesses and generated with different cooling rates.

Young's modulus and other mechanical moduli of films respect to the thickness and applied cooling rate is presented in Fig. 4. The resulting mechanical properties exhibit trends that parallel the morphological features. Films generated with higher cooling rates, which as seen above present reduced numbers of  $sp^3$ - and  $sp^2$ -hybridized atoms, an increased number of homonuclear bonds and higher porosity, display a  $\sim 20\%$  lower Young's modulus compared to samples that were cooled slower. Other moduli values are also decreased significantly with higher cooling rates. High Young's modulus of slow-cooled samples can attributed to high number of  $sp^2$ - and  $sp^3$ -hybridized atoms and absence of pores and voids that we observed in fast-cooled samples. The positive impact of  $sp^3$ -hybridized atoms on mechanical properties is well-established in the

literature [18, 19, 40]. Young’s modulus is particularly critical for diffusion barriers, as a higher value indicates greater stiffness and resistance to deformation. This is essential for ensuring that the barrier maintains its structural integrity during the high-stress conditions typical in semiconductor integration and operation. A higher Young’s modulus in slow-cooled films suggests that these barriers would be better at resisting compressive and tensile stresses, minimizing risks such as cracking or delamination that could compromise the diffusion barrier’s effectiveness. In contrast, the lower Young’s modulus observed in fast-cooled films may render them more susceptible to deformation under stress, which could lead to voids and defects during device fabrication and operation. However, it should be noted that high Young’s modulus in barrier layers could be problematic if there is a mismatch between the thermal expansion coefficients of the barrier and other layers. Since high Young’s modulus leads to more stiff structure, such a mismatch could lead to increased stress and structural deformations.

Although not explicitly shown in the figure, Poisson’s ratio exhibits a weak dependence on applied cooling rates. For films cooled at 5 K/ps and 10 K/ps, Poisson’s ratio remains nearly constant at approximately 0.28–0.30 across different thicknesses, suggesting a consistent balance between lateral expansion and contraction under stress. In contrast, faster-cooled samples exhibit a noticeably lower Poisson’s ratio (0.19–0.22), suggesting a stiffer response to deformation. This change, though subtle, may affect the barrier’s ability to adapt to mechanical strains and its performance during thermal cycling and integration processes.

### *3.3. Dielectric Properties of $\alpha$ -BN Samples*

The use of a low dielectric constant barrier would be desirable compared to current metal barriers, as the absence of a metal barrier increases the cross-sectional area available for low-resistivity metals, such as Cu or other metals with better electromigration characteristics.  $\alpha$ -BN has already been studied for this use [28, 15, 12], however both experimental and theoretical results show a wide range dielectric constant values, strongly suggesting that this property, as well as mechanical and structural properties, depends on the morphology.

In this section, we present the real and imaginary parts of the dielectric functions of the films along the z-direction, which corresponds to the perpendicular to the plane of the thin film. The figure of merit we focus on in this section is the static dielectric constant  $\epsilon_1(\omega = 0)$  of the films.

Fig. 5 shows the z-component of the real and imaginary parts of the dielectric function for 3-nm (a, c) and 5-nm thick (b, d) films.<sup>+</sup> The results are quite similar at both thicknesses. While slow-cooled samples (CR<25 K/ps) at both thicknesses exhibited relatively low dielectric constants, around 2.8 (Fig. 5-a), the dielectric functions of the two fastest-cooled samples displayed a tendency to diverge at low frequencies due to the absence of an electronic gap. Although there seems to be a relationship between

<sup>+</sup> Electronic properties for 7-nm films were not evaluated due to computational limitations.

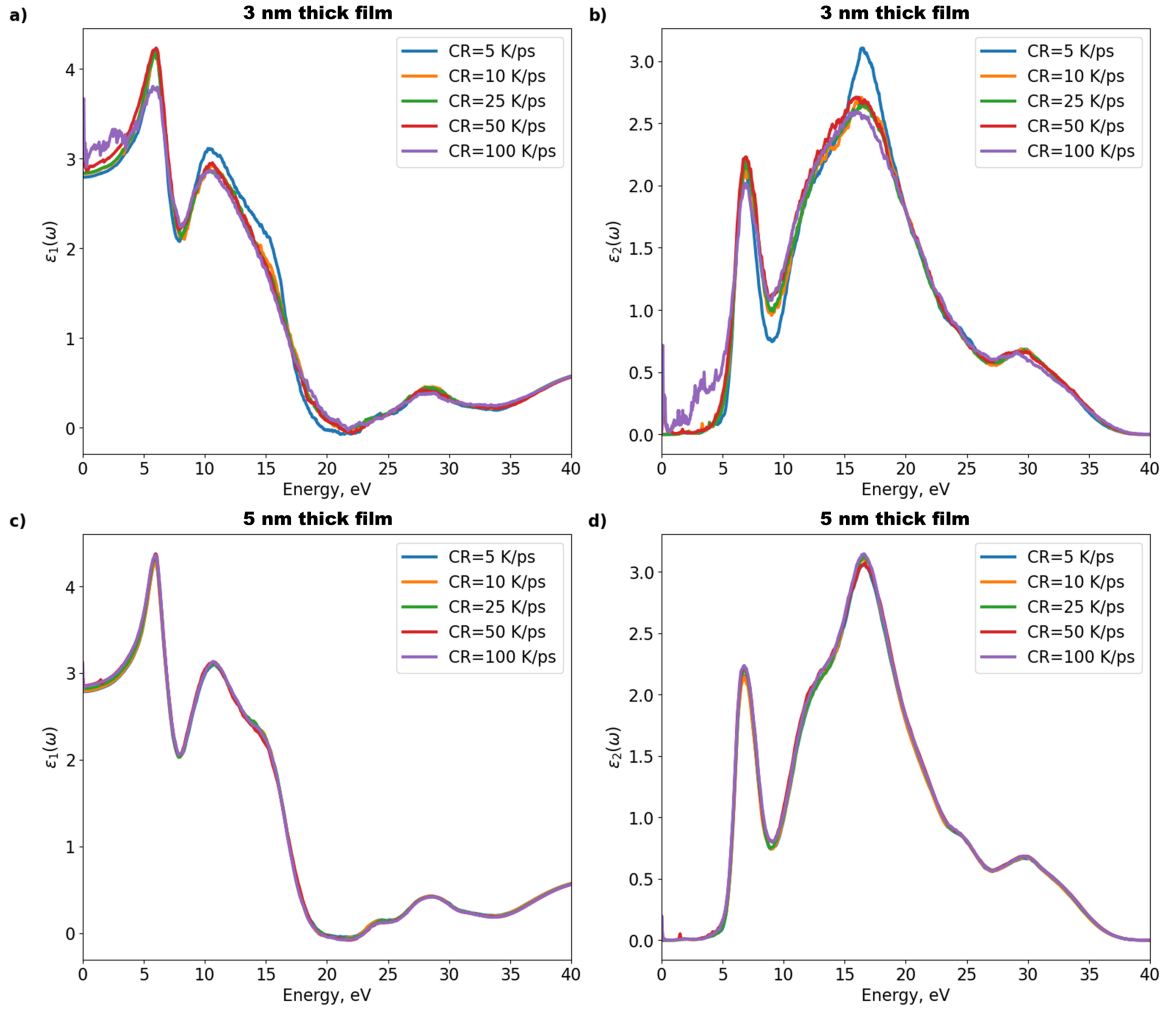


Figure 5: Average real (a,c) and imaginary (b,d) parts of the dielectric function of 3-nm and 5-nm thick  $\alpha$ -BN films along the  $z$  direction as a function of cooling rate.

cooling rates and dielectric constants, the values are too close to establish a definitive trend given the precision of the model.

To better understand these effects, it is of interest to consider the energy and oscillator strengths of electronic transitions in the sample. Indeed,  $\epsilon_1(\omega = 0)$ , up to constants, can be seen as the sum of oscillator strengths over all transition the system, inversely weighted by the transition energies (see equation 1 and, e.g. [28]). Conveniently, the imaginary part of the dielectric function resolves in energy the density and oscillator strengths of electronic transitions (as can be seen from the delta function in equation 2). For fast-cooled samples, it displays peaks at low energies, signaling the existence of low-energy transitions (of non-vanishing oscillator strengths), which are absent in the slowly-cooled samples. To get further insight into these transitions and the dielectric constant behaviours, we examine the DOS and IPR of the films. In Fig. 6, we present, for simplicity, the 3-nm thick films generated with cooling rates of 5 K/ps and 100 K/ps. Both films can be seen to exhibit mid-gap states. However, while the

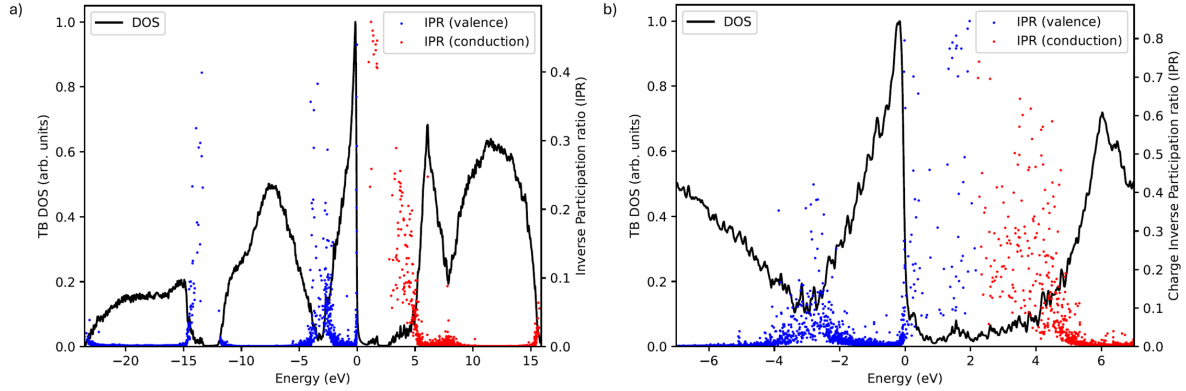


Figure 6: Electronic DOS and inverse participation ratio of 3-nm thick  $\alpha$ -BN samples generated with cooling rates of 5 K/ps (a) and 100 K/ps (b).

slow-cooled sample (6-a) shows a nominal (including mid-gap states) electronic gap of  $\sim 1.2$  eV, the fast-cooled sample (6-b) displays an effectively closed gap, allowing for the aforementioned low-energy transitions. In the slow-cooled sample, it appears that most midgap states are unoccupied (red dots in Fig. (6-a)), while the fast-cooled sample exhibits occupied mid-gap states. In both cases, mid-gap states show  $\text{IPR} > 0$ , indicating real-space localization, which typically suppresses momentum matrix elements between them (numerators in equations 1 and 2) and DC conductivity, lowering (but here not eliminating) their impact on the dielectric constant.

At this point, we must recall the limitations of our electronic model and give further qualitative remarks. In relation to midgap states, DFT calculations in [28] suggest that the dielectric constant of bulk  $\alpha$ -BN is increased by the presence of  $\text{sp}^1$ - and  $\text{sp}^3$ - coordinated atoms (in  $\text{sp}^2$ -dominated samples) and low short range order, which can be related to the presence of homonuclear (B-B and N-N) bonds. Lin et al. [15] also point towards the detrimental effects of Boron clusters. Similarly, Glavin et al. [12] indicated that B-B bonds may promote the formation of mid-gap states or conductive pathways in thin films. These remarks should be put in regard with the findings of section 3.1. We further note that although the sample cooled at 25 K/ps had a significant number of N-N bonds, we did not observe any large N or B clusters. However, we observed some B and N clusters (B-B or N-N bonds with a size of 4-12 atoms). The aforementioned morphological features, which we expect in fast-cooled films; especially in the case of thinner films (see Fig. 3) may contribute to the formation of midgap states and significantly affect the dielectric constant in these films. To a degree, we observe such a trend in the electronic calculations presented here, although the simplicity of the tight-binding model used here may underestimate these effects, making quantitative statements difficult. Finally, we should comment on the effects of density: quickly-cooled films; especially the thinnest ones, present a lower density (Fig. 3 (d)), which favours a lower dielectric constant (see the presence of the unit cell volume in the denominator of equation 1). However, this is accompanied by an increase

in undesirable morphological features ( $sp^1$  fraction, homonuclear bonds). Within the caveats above, our results suggest that the net effect is not favourable for ultralow dielectric constant properties.

#### 4. Theoretical Investigation of $\alpha$ -BN Diffusion Barriers

The effectiveness of  $\alpha$ -BN films as copper diffusion barriers hinges on their ability to resist Cu migration into the barrier structure. This section investigates how the morphology of  $\alpha$ -BN, controlled by cooling protocols and film thickness, influences its diffusion resistance. By studying the interaction of Cu atoms with  $\alpha$ -BN at the atomic scale, we aim to elucidate the structural features critical for preventing copper penetration.

Molecular dynamics (MD) simulations, as described in Section 2.1, were used to model  $\alpha$ -BN/Cu heterostructures.  $\alpha$ -BN films were generated under varying cooling rates to capture a range of disordered morphologies. An annealing protocol, also detailed in Section 2.1, incrementally raised the temperature from 300 K to 1000 K to mimic the experiments presented in Section 5. During this process, the diffusivity of Cu atoms within the  $\alpha$ -BN layer was monitored using MSD calculations, and atomic trajectories were analysed to identify mechanisms and pathways enabling copper diffusion. These simulations provide insights into the interplay between  $\alpha$ -BN morphology and its effectiveness as a diffusion barrier .

Fig. 7 presents the Cu diffusivity as a function of the inverse of temperature within 3-nm (a), 5-nm (b) and 7-nm (c) thick films. We assume that diffusivity of Cu atoms should be negligible as long as the  $\alpha$ -BN barrier can prevent the Cu diffusion. Note that, due to the effects of temperature on atomic motion, diffusivity is expected to increase with temperature (as seen in Fig.7-c), so that only a sharp increase of diffusivity (as seen in Fig.7-b and -c) can be safely interpreted as a sign of barrier failure. All samples, regardless the thickness and morphology, were able to prevent the Cu diffusion at low temperatures. 7-nm thick films prevent or largely mitigate Cu diffusion even at high temperatures (up to 1000 K). In contrast, 3-nm and 5-nm thick films were only successful when lower cooling rates were applied during their formation. As with all properties, the barrier performance of films largely depends on their morphology. Thus, we focused on the morphology of films to better understand the trends shown in Fig. 7. In the case of 7-nm thick films, even films formed with the highest high cooling rates exhibited relatively low levels of  $sp^1$ -hybridized atoms, high density, and fewer nanovoids near the boundaries compared to thinner films. While films cooled rapidly ( $CR > 25$  K/ps) have some voids and  $sp^1$ -hybridized atoms leading to very limited Cu diffusion at near interface, slowly cooled films had a smooth surface without any voids close to the interface, therefore no Cu diffusion. The consistent increase in Cu diffusivity is largely due to increased atomic motion as the temperature increases. The superior diffusion barrier performance of 7-nm films can be attributed to their reduced defects and increased structural order, as described in Section 3.1, which allows them to better resist atomic migration even

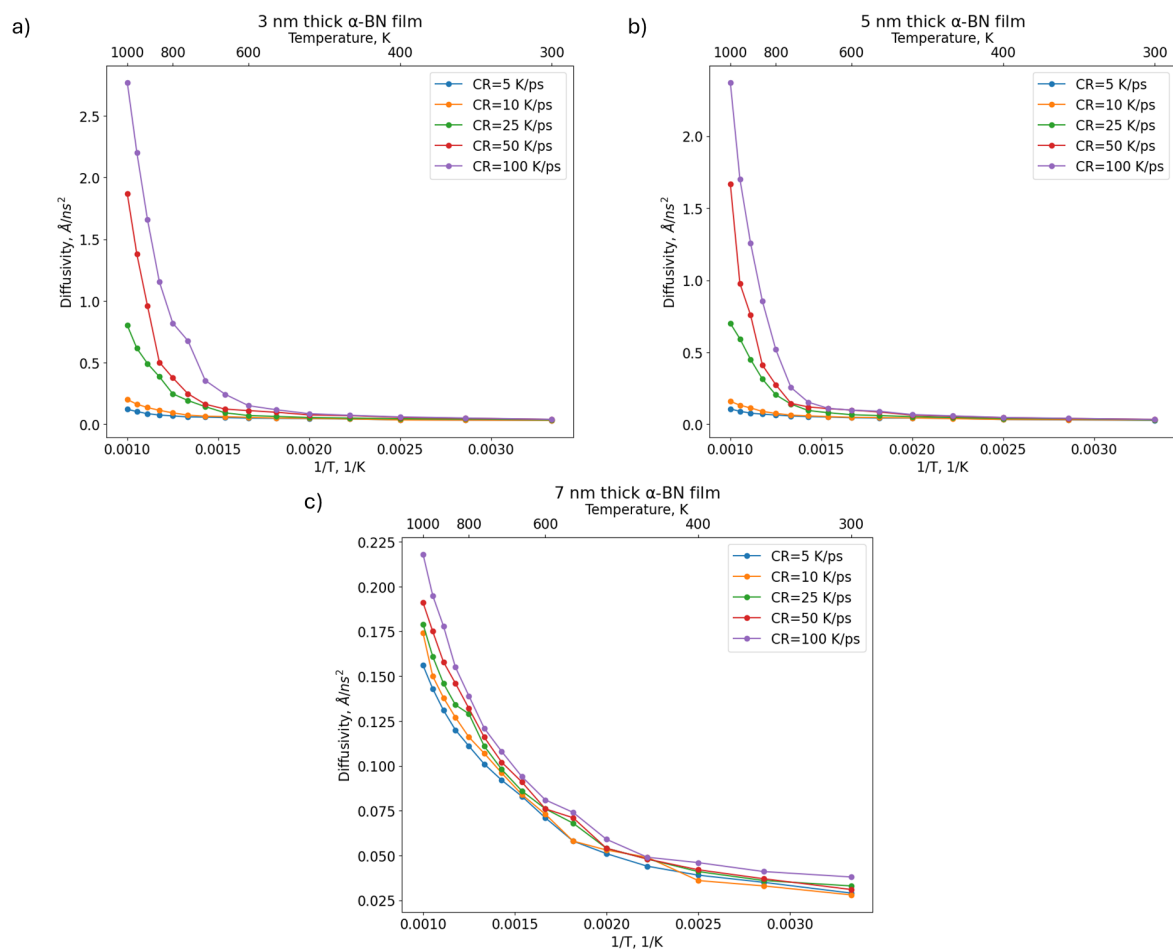


Figure 7: The performance of 3-nm (a), 5-nm (b), and 7-nm (c)  $\alpha$ -BN thick films as diffusion barriers by evaluating the diffusivity,  $D$ , of Cu atoms. A sudden increase in  $D$  is considered as Cu diffusing into the  $\alpha$ -BN film.

under less favourable conditions.

In contrast, the morphology of 3-nm and 5-nm thick films is significantly different than the 7-nm thick films. At higher cooling rates, the proportion of  $sp^1$ -hybridized bonds increased rapidly and voids were observed near the interface between  $\alpha$ -BN and Cu films. Moreover, the surface of rapidly cooled 3-nm and 5-nm thick samples were noticeably rough. The potential energy per atom shows that these films are less stable than the 7-nm thick samples at the same cooling rates, as shown in Fig.B2 in Appendix B, which can be attributed to larger number of  $sp^1$ -hybridized atoms and homonuclear bonds in thinner films. The lower density at high cooling rates (1.9-2.0 for 3-nm and 5-nm thick films,  $\sim 2.1$  for 7-nm thick films at  $CR > 25$  K/ps) along with the other morphological features mentioned here, indicates the existence of the voids in the films cooled rapidly. These voids and  $sp^1$ -hybridized atoms created pathways through the barrier which allowed Cu atoms to diffuse into the  $\alpha$ -BN. While 3-nm and 5-nm films are more susceptible to these defects, films generated at lower cooling rates demonstrated



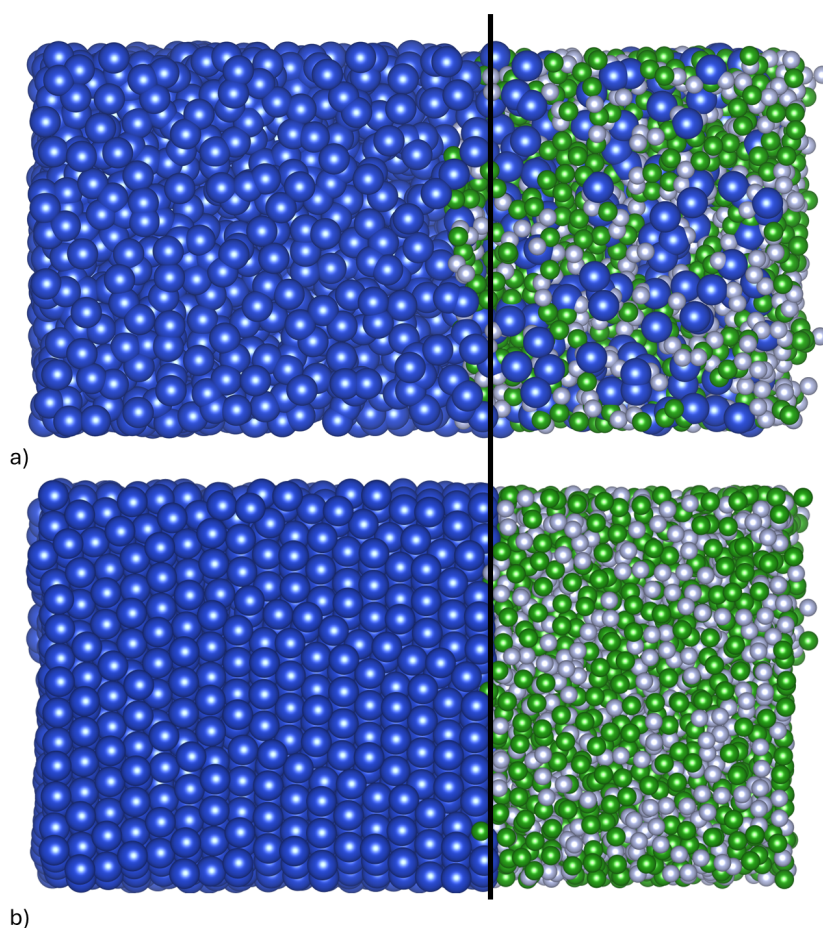


Figure 8: Examples of a failed and successful 3-nm thick  $\alpha$ -BN diffusion barriers against Cu diffusion after the annealing process until 1000 K. While the failed sample was generated using a cooling rate of 100 K/ps (a), a rate of 5 K/ps (b) was applied for the successful one. Black solid line shows the approximate position of the interface before the annealing process.

morphological stability, showing that quality, rather than thickness alone, determines performance. As Cu atoms close to the interface diffused into the  $\alpha$ -BN layer, B and N atoms also migrated into the Cu layer. This process accelerated the void formation and finally  $\alpha$ -BN barriers lost their structural integrity completely. Although providing visual representation of existing voids close to the interface is not easy, we present two 3-nm films which cooled at a rate of 100 K/ps (a) and 5 K/ps (b) in Fig. 8 after the annealing process. The black line shows the initial position of the interface. As shown in the Fig. 8, after the annealing process, the slow-cooled  $\alpha$ -BN barrier stopped Cu atoms from diffusing into the structure (only a few seemed to be diffused into the near interface area, which can be considered negligible). On the other hand, the fast-cooled  $\alpha$ -BN structure contained many small voids and had a worse stability. After the annealing at high temperatures, many Cu atoms diffused into the barrier, causing

it to lose its structural integrity completely. Additionally, some B and N atoms also diffused into the Cu film, although in much smaller quantity compared to the diffused Cu atoms into the  $\alpha$ -BN film. While B and N atoms largely diffused into the regions close to the interface, Cu atoms diffused even deep into the  $\alpha$ -BN. We observed a similar process in other fast-cooled samples (CR: 25-100 K/ps) and 5-nm thick samples as well. However, it should be noted that 5-nm thick films managed to stop Cu diffusion at higher temperatures, however, fast-cooled 5-nm thick films were not able to prevent the Cu diffusion.

These differences in morphology, caused by the different cooling protocols, demonstrate that the barrier performance of the  $\alpha$ -BN films largely depends on the film quality. While 3- and 5-nm thick films generated with cooling rates of 5 K/ps and 10 K/ps could stop the Cu diffusion until 1000 K, films with high coordination defects and voids (cooling rates greater than 50 K/ps) only managed to do the same until 500-600 K. These results suggest that ultrathin  $\alpha$ -BN films, when generated under optimised conditions, can perform comparably to thicker films as effective diffusion barriers and dielectric layers in integrated circuits using Cu wiring.

## 5. Experimental Investigation of $\alpha$ -BN Diffusion Barriers

After we showed the potential of  $\alpha$ -BN films using theoretical models, we conducted an experimental investigation on the diffusion barrier performance of  $\alpha$ -BN films with the same thicknesses we performed our simulations. We fabricated Cu/ $\alpha$ -BN/Si structures and annealed them at 400 - 600 °C for 30 minutes. After annealing at 400 °C, a Si substrate coated with a 3-nm thick  $\alpha$ -BN film did not form any copper silicide (Fig. 9-a), while a Si substrate not covered with  $\alpha$ -BN formed a substantial amount of copper silicide (Fig. 9-e). After annealing 3-nm thick  $\alpha$ -BN/Si at 500 °C, very small copper silicide nucleations were observed on the Si surface (Fig. 9-b), and the formation of copper silicide crystals was confirmed after annealing at 600°C (Fig. 9-d). Fig. 9-c provides a brief summary of Cu diffusion barrier properties of 3-nm, 5-nm, and 7-nm thick  $\alpha$ -BN films after the 400 - 600 °C annealing process. The observation of crystallization by SEM is fine but not sensitive enough to determine Cu diffusion in the sub-silicide formation regime - that is - you could have Cu in the Si but SEM resolution is insufficient to detect or within the solubility limit of Cu in Si (Fig. C1 in Appendix C). The characteristics such as density or existence of defects of experimentally synthesized  $\alpha$ -BN films differ from the simulated  $\alpha$ -BN films and do not exhibit the same barrier performance as the simulations. However, there is a tendency for the barrier property to improve as the thickness of the  $\alpha$ -BN film increases.

## 6. Conclusions

We have investigated the diffusion barrier properties of ultrathin amorphous boron nitride ( $\alpha$ -BN) films against copper penetration by molecular dynamics and supported

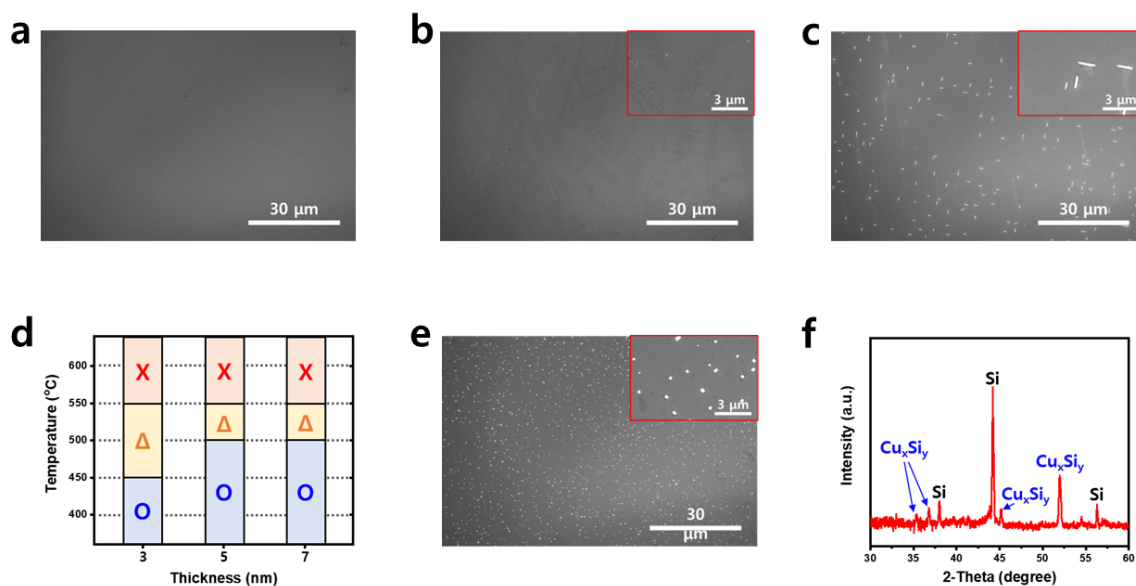


Figure 9: Experimental result of Cu diffusion barrier test. (a-c) SEM images of 3-nm thick  $\alpha$ -BN/Si surface after 400 °C (a), 500 °C (b), and 600 °C (c) annealing and removing residual Cu films with Cu etchants. (d) Evaluation of Cu diffusion barrier properties of 3-nm, 5-nm, and 7-nm thick  $\alpha$ -BN/Si after 400 - 600 °C annealing process. Blue O means  $\alpha$ -BN film successfully blocked Cu diffusion. Yellow Delta means there is small copper silicide nucleation through the defect of  $\alpha$ -BN films. Red X means  $\alpha$ -BN film failed to block Cu diffusion and copper silicide crystals are formed. (e) SEM image of Si surface without  $\alpha$ -BN barrier films after 400 °C annealing and removing residual Cu films with Cu etchants. (f) XRD spectrum of Si surface with copper silicide crystals without  $\alpha$ -BN barrier films that shows the formation of copper silicide crystals.

the simulations with experimental data. We focused on  $\alpha$ -BN films with thicknesses in the few nanometres range, and have analysed the morphologies, mechanical, diffusion barrier and dielectric properties of various  $\alpha$ -BN samples generated by molecular dynamics with machine learning trained interatomic potentials. The theoretical results agree with experimental barrier performance against Cu diffusion measured on PECVD-deposited 3-, 5- and 7-nm thick  $\alpha$ -BN films. Overall, the results confirm that amorphous boron-nitride compounds can be used as a dielectric barrier against Cu diffusion as a way to reduce the time delay in interconnects architectures. Further computational studies of  $\alpha$ -BN with larger thickness are however needed to explore (and find ways to mitigate) the effect of crystallisation observed in experiments, as it could jeopardize reaching the upper performance and integrability of this innovative advanced material into mainstream interconnects technologies. Improved modelling of dielectric properties, beyond the qualitative tight-binding model used here, are likewise needed to better assess the properties of the films for such applications. In addition to a better electronic structure description, a more precise modelling of the dielectric function in the MHz to GHz range (including vibrational and intraband effects) would be of importance

for comparison with experiments and to analyse the behaviour of  $\alpha$ -BN films at device operation frequencies.

## **Acknowledgements**

This project has been supported by Samsung Advanced Institute of Technology and is conducted under the REDI Program, a project that has received funding from the European Union’s Horizon 2020 research and innovation programme under the Marie Skłodowska-Curie grant agreement no. 101034328. This paper reflects only the author’s view and the Research Executive Agency is not responsible for any use that may be made of the information it contains. This work was supported by Institute for Basic Science (IBS-R036-D1), Republic of Korea. ICN2 acknowledges the Grant PCI2021-122092-2A funded by MCIN/AEI/10.13039/501100011033 and by the “European Union NextGenerationEU/PRTR”. H.-J.S. acknowledge support from the National Research Foundation of Korea (NRF) grant funded by the Korea government Ministry of Science and ICT (RS-2024-00352458). Simulations were performed at the Texas Advanced Computing Center (TACC) at The University of Texas at Austin and the Center for Nanoscale Materials, a U.S. Department of Energy Office of Science User Facility, supported by the U.S. DOE, Office of Basic Energy Sciences, under Contract No. DE-AC02-06CH11357.

## **Appendix A. Gaussian Approximation Potentials**

### *Appendix A.1. Generation of the Training Data*

The GAP model used in this study was developed using two sets of samples, “training” and “validation” sets which include positions of atoms, atomic positions, energies, forces, and stresses calculated using Car Parrinello Molecular Dynamics and density functional theory (DFT) with Quantum Espresso package [41, 42, 43]. A multi-step procedure was employed to train the GAP model: 1) large number of amorphous structures were generated using Car-Parrinello MD, 2) the initial training set is generated using DFT calculations, 3) a GAP model is trained over this set; 4) a new set of validation set is generated using the previously generated GAP model; 5) the force and energy estimation of GAP model is evaluated using DFT calculations. These iterative training-validating steps are repeated until sufficiently low RMSE values are reached.

The training and validation sets together contain approximately 4500 structures. Here, the training set was constituted of atomistic structures from different phases of boron nitride, Cu-diffused  $\alpha$ -BN samples,  $\alpha$ -BN/Cu interfaces, and various Cu structures. The densities of all amorphous random samples ( $\alpha$ -B,  $\alpha$ -BN,  $\alpha$ -B<sub>x</sub>N<sub>y</sub>Cu<sub>z</sub>, where x, y and z are random values between 0 and 1, and satisfy the condition  $x + y + z = 1$ ) are set to be between 1.5 - 5.0 g/cm<sup>3</sup>. All amorphous random structures have cubic cells, with the size of the cell determined randomly. Crystalline BN phases (wurtzite, cubic, hexagonal) and Cu phases were (hcp, fcc, bcc, tetragonal) were taken from the

Materials Project database[44]. We also introduced some defects and strain, as well as the melted liquid samples to ensure comprehensive coverage of potential configurations. Once the dataset was generated we randomly split it into training and validation sets which contain 2503 and 2000 structures, respectively. Periodic boundary conditions are applied to the cell for all structures. Ultrasoft pseudopotentials (USPP) with LDA as an exchange-correlation functional have been used for Car-Parrinello MD calculations. The kinetic energy cutoff for wavefunctions and energy are set to 150 Ry and 20 Ry. DFT calculations have been carried out using PAW pseudopotentials with PBE exchange-correlation functionals. Energy cutoffs of 75 Ry and 600 Ry have been employed for the wavefunction and electron density, respectively. To account for the van der Waals (vdW) interactions between BN/Cu interfaces, the non-local vdw-df-obk8 functionals[45] were used. A Gaussian smearing of 0.1 eV width is applied to electronic levels. Car-Parrinello MD simulations were performed using  $\Gamma$ -point sampling, while DFT calculations were performed using Monkhorst-Pack grids of 8x8x8 for 3D samples and 8x8x1 for monolayer samples.

The GAP model is trained using the QUIP software [46, 20]. We employed three descriptors: two-body(2b), three-body(3b), and smooth overlap of atomic positions (SOAP). The 2b descriptor is used to describe the pairwise interactions between atoms. The 3b and SOAP descriptors represent the contribution of the atomic triplets and the local environment around an atom. The cut-offs and hyperparameters for each descriptor have been presented in Table A1. The GAP models have been proven to be useful for several materials [18, 19, 22, 47]. Sparsification using the CUR method [48] was selected for the SOAP kernel, while sparsification on a uniform grid was used for two-body and three-body kernels. The quality of the trained GAP model was later assessed by comparing the obtained energies per atom and forces of samples in the training and validation sets with the trained GAP model and DFT calculations. The root-mean-square errors for energy and forces on training data are 0.0029 eV/atom and 0.296 eV/Å and on validation data are 0.0031 eV/atom and 0.306 eV/Å, as shown in Fig. A1. The obtained RMSE values are similar to the values in the literature for similar amorphous structures [49, 22, 50]. Given that amorphous materials and complex systems, like the one we presented this study, require a highly diverse dataset, the RMSE values are considered as acceptable[50].

A slightly higher RMSE for the validation set is expected since those structures are not used for training the model. Low RMSE values show a good agreement between the GAP model and DFT calculations.

To further validate the potential, we calculated the average bond lengths of h-BN and Cu (111) slabs using both DFT calculations and GAP potentials by relaxing the structures. We also calculated the average interlayer distance between hBN and FCC Cu. For DFT relaxation, the same pseudopotentials and cutoffs used to generate the dataset were applied. The results show excellent agreement between DFT and GAP. The average bond length between B and N atoms in hBN was measured as 1.450 Å with GAP-MD and 1.447 Å with DFT, while the interatomic distance between Cu atoms was calculated

as 2.540 Å using GAP-MD and 2.534 Å using DFT. These values are not only consistent with each other but also with reported values in the literature [51, 52, 18]. The interlayer distance between hBN and Cu was calculated as approximately 3.327 Å using GAP-MD, while ab-initio MD simulations produced an interlayer distance of 3.332 Å. Reported interlayer distances between hBN and Cu in the literature range from 2.44 Å to 3.34 Å [53, 54, 55, 56, 57]. This variation can be attributed to differences in functionals, pseudopotentials, or software. However, both GAP-MD and ab-initio MD results fall within this range, demonstrating the reliability of the potential.

	2-body	3-body	SOAP
$\delta$ (eV)	2.0	0.1	0.1
$r_{cut}$ (Å)	4.0	3.2	7.0
$r_{\Delta}$ (Å)			0.5
$\sigma_{at}$ (Å)			0.5
$n_{max}, l_{max}$			8, 8
$\zeta$			4
Sparsification	Uniform	Uniform	CUR
$N_t$ ( $\alpha$ -BN/Cu samples)		150	3000
$N_t$ (Crystalline samples)		50	1000
$N_t$ (Total)	25	200	4000

Table A1: Parameters used to train the GAP potential for  $\alpha$ -BN/Cu heterostructures.

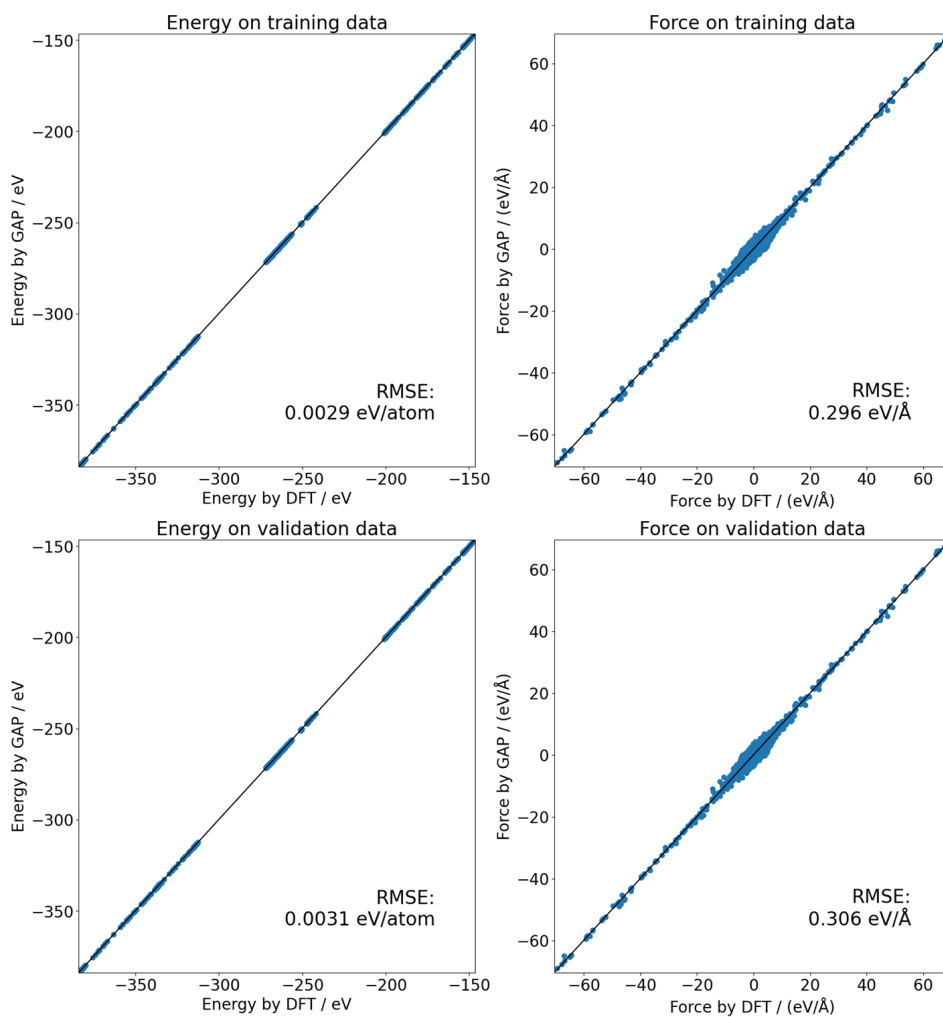


Figure A1: RMSE of energy and forces on training and validation sets.

## Appendix B. Additional Morphological Information

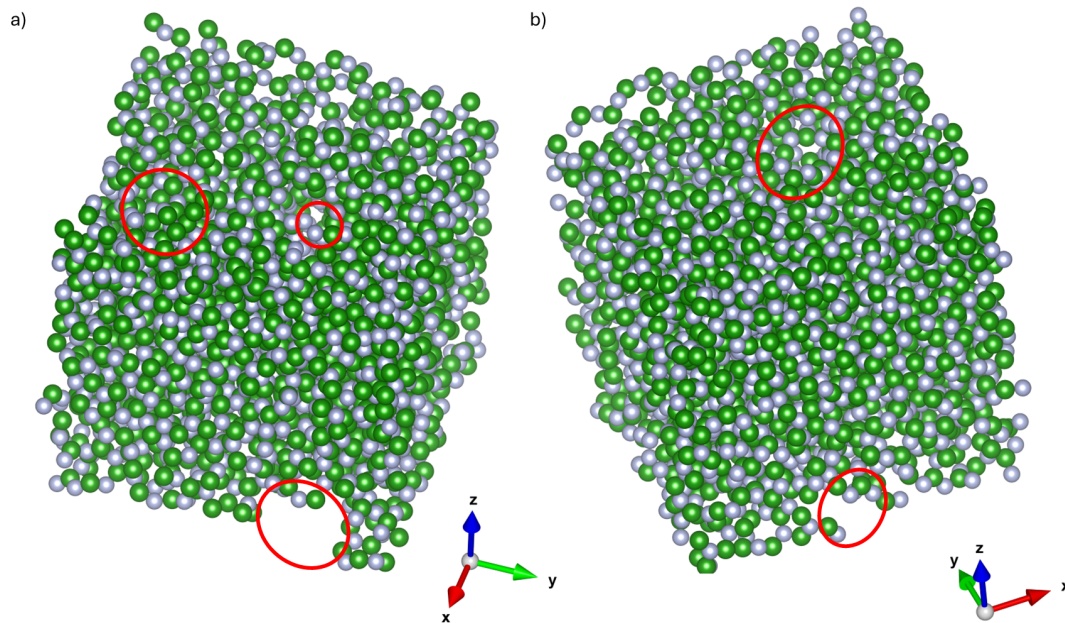


Figure B1: Nanovoids and pinholes observed in one of the 3-nm thick  $\alpha$ -BN sample. The both image belongs to the same sample, they are tilted to show the nanovoids and pinholes within the structure. With high cooling rates, such defects were formed in  $\alpha$ -BN samples. Large number of the atoms surrounding these nanovoids and pinholes are mostly  $sp^1$ -hybridized (have coordination number:2).



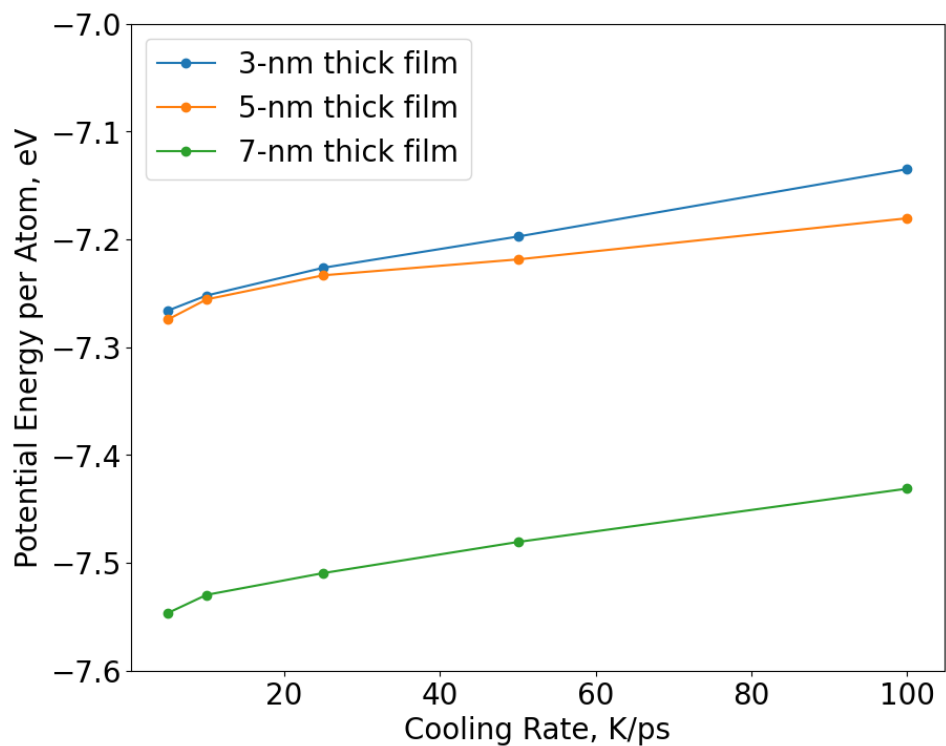


Figure B2: Potential energy per atom with respect to cooling rates and thicknesses of the films. This is a further parameter we used to evaluate the stability of the films. Moreover, the potential energy values increased with larger cooling rates that we applied to generate  $\alpha$ -BN films. This visualizes the impact of cooling rate on the stability of films.

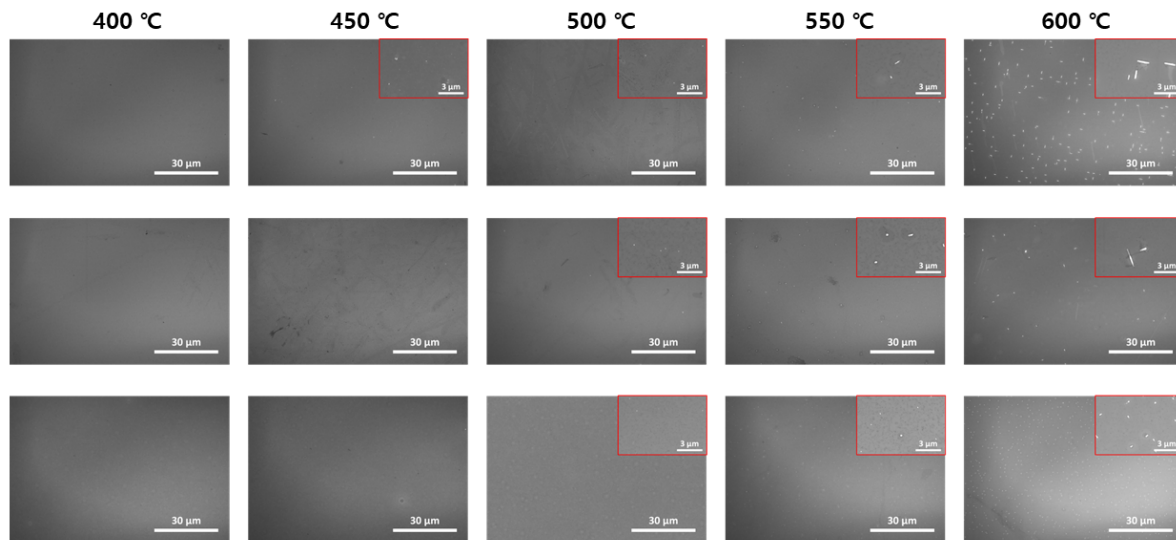
Appendix C. SEM Images of  $\alpha$ -BN Diffusion Barriers

Figure C1: SEM images of 3-nm, 5-nm, and 7-nm thick  $\alpha$ -BN/Si after 400–600 °C annealing and removing residual Cu films with Cu etchants. The insets boxed in red represent enlarged images of the copper silicide.

## References

- [1] Shamiryan D, Abell T, Iacopi F and Maex K 2004 *Materials Today* **7** 34–39 ISSN 1369-7021 URL <https://www.sciencedirect.com/science/article/pii/S1369702104000537>
- [2] Hong S, Lee C S, Lee M H, Lee Y, Ma K Y, Kim G, Yoon S I, Ihm K, Kim K J, Shin T J, Kim S W, Chae Jeon E, Jeon H, Kim J Y, Lee H I, Lee Z, Antidormi A, Roche S, Chhowalla M, Shin H J and Shin H S 2020 *Nature* **582**(7813) 511–514 ISSN 1476-4687 URL <https://doi.org/10.1038/s41586-020-2375-9>
- [3] Liu J, Loh K P, Lin M, Foo Y L, Wang W D and Chi D Z 2004 *Journal of Applied Physics* **96** 6679–6684 ISSN 0021-8979 (Preprint [https://pubs.aip.org/aip/jap/article-pdf/96/11/6679/14681778/6679\\_1\\_online.pdf](https://pubs.aip.org/aip/jap/article-pdf/96/11/6679/14681778/6679_1_online.pdf)) URL <https://doi.org/10.1063/1.1808909>
- [4] Lo C L, Zhang K, Scott Smith R, Shah K, Robinson J A and Chen Z 2018 *IEEE Electron Device Letters* **39** 873–876
- [5] Deijkers J S H, de Jong A A, Mattinen M J, Schulpen J J P M, Verheijen M A, Sprey H, Maes J W, Kessels W E M M, Bol A A and Mackus A J M 2023 *Advanced Materials Interfaces* **10** 2202426 (Preprint <https://onlinelibrary.wiley.com/doi/pdf/10.1002/admi.202202426>) URL <https://onlinelibrary.wiley.com/doi/abs/10.1002/admi.202202426>
- [6] Zhao R, Lo C L, Zhang F, Ghosh R K, Knobloch T, Terrones M, Chen Z and Robinson J 2019 *Advanced Materials Interfaces* **6** 1901055 (Preprint <https://onlinelibrary.wiley.com/doi/pdf/10.1002/admi.201901055>) URL <https://onlinelibrary.wiley.com/doi/abs/10.1002/admi.201901055>
- [7] Maestre C, Toury B, Steyer P, Garnier V and Journet C 2021 *Journal of Physics: Materials* **4** 044018 URL <https://dx.doi.org/10.1088/2515-7639/ac2b87>
- [8] Ranjan A, O'Shea S J, Padovani A, Su T, La Torraca P, Ang Y S, Munde M S, Zhang C, Zhang X, Bosman M, Raghavan N and Pey K L 2023 *ACS Applied Electronic Materials* **5** 1262–1276

- [9] Jiang L, Shi Y, Hui F, Tang K, Wu Q, Pan C, Jing X, Uppal H, Palumbo F, Lu G, Wu T, Wang H, Villena M A, Xie X, McIntyre P C and Lanza M 2017 *ACS Applied Materials & Interfaces* **9** 39758–39770 pMID: 29039199
- [10] Ahmed M, Li Y, Chen W and Li E P 2022 *Nanotechnology* **33** 165201 URL <https://dx.doi.org/10.1088/1361-6528/ac4879>
- [11] Glavin N R, Jespersen M L, Check M H, Hu J, Hilton A M, Fisher T S and Voevodin A A 2014 *Thin Solid Films* **572** 245–250 ISSN 0040-6090 the 41st International Conference on Metallurgical Coatings and Thin Films URL <https://www.sciencedirect.com/science/article/pii/S004060901400813X>
- [12] Glavin N R, Muratore C, Jespersen M L, Hu J, Hagerty P T, Hilton A M, Blake A T, Grabowski C A, Durstock M F, McConney M E, Hilgefort D M, Fisher T S and Voevodin A A 2016 *Advanced Functional Materials* **26**(16) 2640–2647 URL <https://onlinelibrary.wiley.com/doi/abs/10.1002/adfm.201505455>
- [13] Sattari-Esfahlan S M, Kim H G, Hyun S H, Choi J H, Hwang H S, Kim E T, Park H G and Lee J H 2023 *ACS Applied Materials and Interfaces* **15**(5) 7274–7281 ISSN 19448252
- [14] Chen C Y, Sun Z, Torsi R, Wang K, Kachian J, Liu B, Rayner Jr G B, Chen Z, Appenzeller J, Lin Y C *et al.* 2023 *arXiv preprint arXiv:2312.09136*
- [15] Lin C M, Hsu C H, Huang W Y, Astié V, Cheng P H, Lin Y M, Hu W S, Chen S H, Lin H Y, Li M Y, Magyari-Kope B, Yang C M, Decams J M, Lee T L, Gui D, Wang H, Woon W Y, Lin P, Wu J, Lee J J, Liao S S and Cao M 2022 *Advanced Materials Technologies* **7**(10) 2200022 URL <https://onlinelibrary.wiley.com/doi/abs/10.1002/admt.202200022>
- [16] Abbas Q, Liang H, Shi J, Chen Y, Xia X, ul Ahmad A, Liu J and Du G 2018 *Materials Letters* **227** 284–288 ISSN 0167-577X URL <https://www.sciencedirect.com/science/article/pii/S0167577X1830853X>
- [17] Kim K, Kim H, Lee S W, Lee M Y, Lee G, Park Y, Kim H, Lee Y H, Kim M, Ma K Y, Kim M J, Kim T S, Shin H S and Cho B J 2023 *IEEE Transactions on Electron Devices* **70**(5) 2588–2593 ISSN 0018-9383 URL <https://ieeexplore.ieee.org/document/10079183/>
- [18] Kaya O, Colombo L, Antidormi A, Lanza M and Roche S 2023 *Nanoscale Horizons* **8**(3) 361–367 ISSN 20556764
- [19] Kaya O, Colombo L, Antidormi A, Villena M A, Lanza M, Cole I and Roche S 2024 *Journal of Physics: Materials* **7** 025010
- [20] Bartók A P, Payne M C, Kondor R and Csányi G 2010 *Physical Review Letters* **104**(13) 136403 URL <https://link.aps.org/doi/10.1103/PhysRevLett.104.136403>
- [21] Bartók A P, Kondor R and Csányi G 2013 *Phys. Rev. B* **87**(18) 184115 URL <https://link.aps.org/doi/10.1103/PhysRevB.87.184115>
- [22] Deringer V L and Csányi G 2017 *Physical Review B* **95**(9) ISSN 24699969
- [23] Clavier G and Thompson A P 2023 *Computer Physics Communications* **286** 108674 ISSN 0010-4655 URL <https://www.sciencedirect.com/science/article/pii/S001046552300019X>
- [24] Zhen Y and Chu C 2012 *Computer Physics Communications* **183** 261–265 ISSN 0010-4655 URL <https://www.sciencedirect.com/science/article/pii/S0010465511003249>
- [25] Clavier G, Desbiens N, Bourasseau E, Lachet V, Brusselle-Dupend N and Rousseau B 2017 *Molecular Simulation* **43** 1413–1422
- [26] Ray J R and Rahman A 1984 *The Journal of Chemical Physics* **80** 4423–4428 ISSN 0021-9606 (*Preprint* [https://pubs.aip.org/aip/jcp/article-pdf/80/9/4423/9721933/4423\\_1\\_online.pdf](https://pubs.aip.org/aip/jcp/article-pdf/80/9/4423/9721933/4423_1_online.pdf)) URL <https://doi.org/10.1063/1.447221>
- [27] Zhou X W, El Gabaly F, Stavila V and Allendorf M D 2016 *The Journal of Physical Chemistry C* **120** 7500–7509 (*Preprint* <https://doi.org/10.1021/acs.jpcc.6b01802>) URL <https://doi.org/10.1021/acs.jpcc.6b01802>
- [28] Galvani T, Hamze A K, Caputo L, Kaya O, Dubois S M, Colombo L, Nguyen V H, Shin Y, Shin H J, Charlier J C and Roche S 2024 *Journal of Physics: Materials* **7** 035003
- [29] Grosso G and Parravicini G P 2013 *Solid state physics* (Academic press)

- [30] Cudazzo P, Tokatly I V and Rubio A 2011 *Physical Review B—Condensed Matter and Materials Physics* **84** 085406
- [31] Graf M and Vogl P 1995 *Physical Review B* **51** 4940
- [32] Boykin T B, Bowen R C and Klimeck G 2001 *Physical Review B* **63** 245314
- [33] Boykin T B and Vogl P 2001 *Physical Review B* **65** 035202
- [34] Delerue C J and Lannoo M 2013 *Nanostructures: theory and modeling* (Springer Science & Business Media)
- [35] Agirseven O, Biswas P and Tate J 2022 *Journal of Materials Research* **37** 1135–1143 ISSN 2044-5326 URL <https://doi.org/10.1557/s43578-021-00478-x>
- [36] Moghadam M, Pang E, Philippe T and Voorhees P 2016 *Thin Solid Films* **612** 437–444 ISSN 0040-6090 URL <https://www.sciencedirect.com/science/article/pii/S0040609016302796>
- [37] Trofimov V I, Trofimov I V and Kim J I 2006 *Thin Solid Films* **495** 398–403 ISSN 0040-6090 eMRS 2005 Symposium E URL <https://www.sciencedirect.com/science/article/pii/S0040609005014665>
- [38] Framil D, Van Gompel M, Bourgeois F, Furno I and Leterrier Y 2019 *Frontiers in Materials* **6** 319
- [39] Wang Y, Moitreyee M, Kumar R, Wu S, Xie J, Yew P, Subramanian B, Shen L and Zeng K 2004 *Thin Solid Films* **462** 227–230
- [40] Jana R, Savio D, Deringer V L and Pastewka L 2019 *Modelling and Simulation in Materials Science and Engineering* **27**(8) 85009 URL <https://dx.doi.org/10.1088/1361-651X/ab45da>
- [41] Giannozzi P, Baroni S, Bonini N, Calandra M, Car R, Cavazzoni C, Ceresoli D, Chiarotti G L, Cococcioni M, Dabo I *et al.* 2009 *Journal of physics: Condensed matter* **21** 395502
- [42] Giannozzi P, Andreussi O, Brumme T, Bunau O, Nardelli M B, Calandra M, Car R, Cavazzoni C, Ceresoli D, Cococcioni M *et al.* 2017 *Journal of physics: Condensed matter* **29** 465901
- [43] Giannozzi P, Baseggio O, Bonfà P, Brunato D, Car R, Carnimeo I, Cavazzoni C, De Gironcoli S, Delugas P, Ferrari Ruffino F *et al.* 2020 *The Journal of Chemical Physics* **152** 154105
- [44] Jain A, Ong S P, Hautier G, Chen W, Richards W D, Dacek S, Cholia S, Gunter D, Skinner D, Ceder G and Persson K A 2013 *APL Materials* **1** 011002 ISSN 2166-532X (*Preprint* [https://pubs.aip.org/aip/apm/article-pdf/doi/10.1063/1.4812323/13163869/011002\\_1\\_online.pdf](https://pubs.aip.org/aip/apm/article-pdf/doi/10.1063/1.4812323/13163869/011002_1_online.pdf)) URL <https://doi.org/10.1063/1.4812323>
- [45] Klimeš J, Bowler D R and Michaelides A 2009 *Journal of Physics: Condensed Matter* **22** 022201 URL <https://dx.doi.org/10.1088/0953-8984/22/2/022201>
- [46] Csányi G, Winfield S, Kermodé J R, De Vita A, Comisso A, Bernstein N and Payne M C 2007 *IoP Comput. Phys. Newsletter* Spring 2007
- [47] Deringer V L, Bartók A P, Bernstein N, Wilkins D M, Ceriotti M and Csányi G 2021 Gaussian process regression for materials and molecules
- [48] Mahoney M W and Drineas P 2009 *Proceedings of the National Academy of Sciences* **106** 697–702
- [49] Sivaraman G, Krishnamoorthy A N, Baur M, Holm C, Stan M, Csányi G, Benmore C and Álvaro Vázquez-Mayagoitia 2020 *npj Computational Materials* **6**(1) ISSN 20573960
- [50] Fujikake S, Deringer V L, Lee T H, Krynski M, Elliott S R and Csányi G 2018 *The Journal of Chemical Physics* **148**(24) 241714 ISSN 0021-9606 URL <https://doi.org/10.1063/1.5016317>
- [51] Shinde P P, Tagade P, Adiga S P, Konar A, Pandian S, Mayya K S, Shin H J, Cho Y and Park S 2020 *Phys. Rev. B* **102**(16) 165102 URL <https://link.aps.org/doi/10.1103/PhysRevB.102.165102>
- [52] Wolloch M, Feldbauer G, Mohn P, Redinger J and Vernes A 2014 *Phys. Rev. B* **90**(19) 195418 URL <https://link.aps.org/doi/10.1103/PhysRevB.90.195418>
- [53] Lyalin A, Nakayama A, Uosaki K and Taketsugu T 2014 *Topics in catalysis* **57** 1032–1041
- [54] Brülke C, Heepenstrick T, Humberg N, Krieger I, Sokolowski M, Weiß S, Tautz F S and Soubatch S 2017 *The Journal of Physical Chemistry C* **121** 23964–23973 (*Preprint* <https://doi.org/10.1021/acs.jpcc.7b06107>) URL <https://doi.org/10.1021/acs.jpcc.7b06107>
- [55] Feigelson B N, Bermudez V M, Hite J K, Robinson Z R, Wheeler V D, Sridhara K and Hernández S C 2015 *Nanoscale* **7**(8) 3694–3702 URL <http://dx.doi.org/10.1039/C4NR05557H>

- [56] Lin S, Huang J and Gao X 2015 *Phys. Chem. Chem. Phys.* **17**(34) 22097–22105 URL <http://dx.doi.org/10.1039/C5CP03027G>
- [57] Koitz R, Seitsonen A P, Iannuzzi M and Hutter J 2013 *Nanoscale* **5**(12) 5589–5595 URL <http://dx.doi.org/10.1039/C3NR00709J>